

A Comparison of Barostats for the Mechanical Characterization of Metal–Organic Frameworks

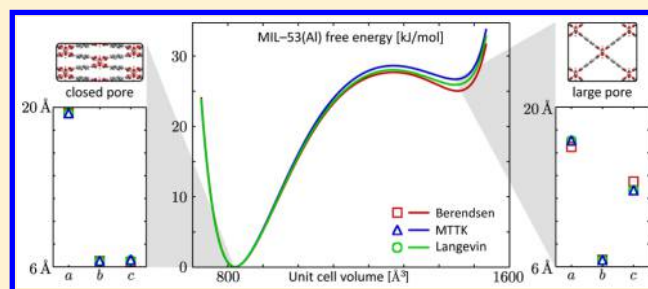
S.M.J. Rogge,[†] L. Vanduyfhuys,[†] A. Ghysels,[†] M. Waroquier,[†] T. Verstraelen,[†] G. Maurin,[‡] and V. Van Speybroeck^{*,†}

[†]Center for Molecular Modeling (CMM), Ghent University, Technologiepark 903, 9052 Zwijnaarde, Belgium

[‡]Institut Charles Gerhardt Montpellier, Université Montpellier 2, Place Eugène Bataillon, 34095 Montpellier cedex 05, France

S Supporting Information

ABSTRACT: In this paper, three barostat coupling schemes for pressure control, which are commonly used in molecular dynamics simulations, are critically compared to characterize the rigid MOF-5 and flexible MIL-53(Al) metal–organic frameworks. We investigate the performance of the three barostats, the Berendsen, the Martyna–Tuckerman–Tobias–Klein (MTTK), and the Langevin coupling methods, in reproducing the cell parameters and the pressure versus volume behavior in isothermal–isobaric simulations. A thermodynamic integration method is used to construct the free energy profiles as a function of volume at finite temperature. It is observed that the aforementioned static properties are well-reproduced with the three barostats. However, for static properties depending nonlinearly on the pressure, the Berendsen barostat might give deviating results as it suppresses pressure fluctuations more drastically. Finally, dynamic properties, which are directly related to the fluctuations of the cell, such as the time to transition from the large-pore to the closed-pore phase, cannot be well-reproduced by any of the coupling schemes.



1. INTRODUCTION

Molecular dynamics (MD) simulations have proven to be an indispensable tool for gaining insight into the microscopic behavior of a broad range of materials and are widely used to characterize, among others, biomolecules and nanoporous materials.^{1–3} Although the most basic MD algorithm solves Hamilton's classical equations of motion and predicts properties in the microcanonical ensemble,⁴ most experiments are carried out under constant temperature and pressure. Hence, thermostat and barostat algorithms are introduced in the MD simulation to explicitly control the temperature and the pressure, respectively. A variety of different algorithms exists based on different equations of motion to perturb the original system and to yield properties at constant temperature and/or pressure. However, these perturbations might lead to non-physical artifacts, as was shown in recent critical assessments on the use of thermostats.^{5–8} For barostats, prior work indicated that not all barostats predict the correct volume distribution for isotropic systems,⁹ but it was not further investigated how this affects the simulation results. Herein, such a study is presented, and a critical comparison is made on the influence of barostats on the properties of metal–organic frameworks.

Temperature control in MD simulations was initiated by Turq et al. in 1977, who applied the principle of Brownian motion to cool down a system and in this way obtained the Langevin equations.¹⁰ These equations were later generalized by the group of Parrinello with the help of the canonical sampling through velocity rescaling (CSVR) thermostat^{11–14}

and colored-noise thermostat,^{15–17} increasing both the efficiency and the applicability of the simulations. In addition, pioneering work was performed by Andersen, who introduced stochastic collisions to equilibrate the temperature,¹⁸ and by Berendsen et al., who proposed a completely deterministic method to control the temperature.¹⁹ Another deterministic approach was also independently followed by Hoover et al.,²⁰ Evans and Morriss,²¹ and Haile and Gupta,²² whose ideas were combined in the so-called Nosé thermostat.^{23,24} In this thermostat, Nosé introduced a unified formulation to control the temperature deterministically by extending the original system with an additional thermostat degree of freedom. This idea was reformulated by Hoover, resulting in the well-known Nosé–Hoover thermostat,²⁵ and extended by Nosé allowing for the thermostat to couple differently to the various degrees of freedom of the system.²⁶ Martyna et al. introduced additional thermostat degrees of freedom in the so-called Nosé–Hoover chains,²⁷ which were recently extended to form Nosé–Hoover networks by Morishita.²⁸ Although we will concentrate on the Langevin, Berendsen, and Nosé–Hoover chain thermostats, it should be observed that the quest for new thermostats is still ongoing. Noteworthy results may be found in nonequilibrium simulations using dissipative particle dynamics,²⁹ faster equilibration techniques with the aid of log oscillators,³⁰ and

Received: August 5, 2015

Published: October 23, 2015

advanced coupling methods between the thermostat and the original system.³¹

Likewise, a plethora of barostats exists, starting with the work of Parrinello and Rahman,^{32,33} which was further explored by Nosé and Klein.³⁴ However, it was shown that the resulting equations of motion depend on the initial cell orientation, which is undesirable.^{35,36} Independently, Andersen,¹⁸ Berendsen et al.,¹⁹ and Hoover^{25,37} developed deterministic barostats. The Hoover barostat was extended to account for fluctuations in both cell shape and volume by Melchionna et al.³⁸ It was later observed by Martyna et al. that the proposed equations of motion were only correct in the limit of large systems. To account for this, they introduced their own equations in the Martyna–Tuckerman–Tobias–Klein (MTTK) barostat,^{39,40} which will be employed and tested in this work. Finally, the idea of the Langevin thermostat was extended to achieve pressure control, first by only scaling the volume of the system,⁹ but later on by also allowing the cell shape to fluctuate.⁴¹ Because these barostats affect the equations of motion, it is of the utmost importance to understand the influence of the various coupling schemes on the prediction of properties for different materials.

In this work, we will use and compare three of these barostat implementations, the Berendsen, MTTK, and Langevin barostats, for the simulation of metal–organic frameworks (MOFs), a specific class of nanoporous materials consisting of metal oxides interconnected by organic linkers. These materials are envisaged to play an important role in applications such as gas storage, separation, catalysis, and controlled drug release.^{42–45} Although the synthesis of MOFs started only two decades ago,^{46–50} a continuously expanding set of MOFs is being examined today to find the ideal candidate for the aforementioned applications.^{51–57} However, for any of these applications, a mechanical characterization of the MOF is a prerequisite. Indeed, before a MOF can be used as a porous catalyst material in a reactor, the MOF powder needs to be shaped, which involves pressures on the order of several GPa.⁵⁸ Moreover, flexible MOFs are also promising for the absorption of shocks or for the storage of other forms of mechanical energy because of their structural transitions at moderate pressures of several tens of MPa.^{59–64} Thus, to further aid their development, a complete understanding of the mechanical behavior of MOFs over a broad range of pressures is essential.

In this article, two prototype materials are highlighted. The first material, the highly flexible MIL-53(Al), consists of aluminum oxide chains, which are interconnected by benzenedicarboxylate (BDC) linkers. This material exhibits two phases, the closed-pore (CP) and the large-pore (LP) phase, with a relative volume difference of 38% and belonging to a different symmetry group. For MIL-53-type materials, transitions between the two phases can be triggered by changing their relative stability through external parameters, such as temperature,^{64,65} pressure,^{59,63,64,66} and gas or liquid exposure.^{55,56} Hence, MD simulations on MIL-53(Al) might critically depend on the applied thermostat and barostat. The second material at hand is MOF-5,⁴⁶ a rigid structure composed of zinc oxide centers and phenyl linkers. MOF-5 is renowned for its negative thermal expansion coefficient,⁶⁷ and its predicted bulk modulus is verified based on experimental and computational studies.^{68,69}

MD simulations have proven to be an essential tool in the fundamental understanding of the structural behavior of these solids upon diverse stimuli and of the dynamics of guest

molecules confined in their pores. Ford et al. determined the self-diffusion of chain molecules in MOF-5,⁷⁰ whereas Rosenbach et al., Salles et al., and Babarao and Jiang studied diffusion of light hydrocarbons and CO₂ in MIL-47(V), MIL-53(Al), and MIL-53(Cr).^{71–74} For MIL-53(Cr), Paesani also investigated the process of water-mediated proton transport.⁷⁵ All of these theoretical investigations were carried out in the (N,V,T) ensemble with different thermostat implementations, some of which were shown to give erroneous results.⁸ Several studies also report on MD simulations carried out in the (N,P,T) ensemble, such as the work of Greathouse et al. on the cell parameters of MOF-5 when immersed in water,⁷⁶ and the work of Tafipolsky and Schmid in a validation of a force-field development protocol for MOFs.⁷⁷ Further, (N,P,T) simulations have been performed by Yot et al. to investigate the breathing behavior of MIL-47(V) and MIL-53(Al) under the influence of pressure,^{59,62} as well as by Ghoufi and Maurin in their hybrid osmotic Monte Carlo scheme.⁷⁸ Except for the simulations in ref 76, where an MTTK barostat has been employed, all other works employ the Berendsen pressure coupling method. To reliably predict different properties of these challenging materials, it is necessary to compare and validate results obtained with different barostats. This is precisely the aim of this work. We will make a distinction between static properties, such as cell lengths and equilibrium geometries, and dynamic properties, such as the rate at which the aforementioned structural transitions occur.

This work is organized as follows. In section 2, a more precise notation is introduced to describe various thermodynamic ensembles. Next, an overview of the three barostats in this work, the Berendsen, MTTK, and Langevin barostats, is given with a focus on the differences in their mechanisms. Also, the methodology to derive the mechanical properties of interest is outlined. After stating the computational details in section 3, the different barostats are applied in three distinct applications (section 4). First, the reproduction of the unit cell parameters for the stable state of MOF-5 and the CP and LP structural phases in MIL-53(Al) is discussed with a selection of the relevant internal coordinates to characterize the structural transformation in MIL-53(Al) (section 4.1). Second, internal pressure versus volume profiles are constructed. From these profiles, the transition pressure can be determined, and using a thermodynamic integration method, the free energy versus volume profiles may be constructed (section 4.2). In a third application, the transition pressure is derived via a dynamical analysis in section 4.3. Finally, in section 5, concluding remarks are made concerning the use of the different barostats, which are especially relevant when simulating metal–organic frameworks.

2. THEORY

2.1. Thermodynamic Ensembles. To fully describe the size and shape modifications of flexible materials such as MOFs, it is essential to introduce a unit cell tensor \mathbf{h} that contains the three unit cell vectors \mathbf{a} , \mathbf{b} , and \mathbf{c} , as shown in Figure 1. The unit cell tensor can be split into the cell volume $V = \det(\mathbf{h})$ and a normalized unit cell tensor \mathbf{h}_0 with $\det(\mathbf{h}_0) = 1$:

$$\mathbf{h} = V^{1/3} \mathbf{h}_0 \quad (1)$$

In the general three-dimensional case, the unit cell tensor \mathbf{h} contains nine degrees of freedom. Three of them describe the orientation of the cell with respect to the chosen reference

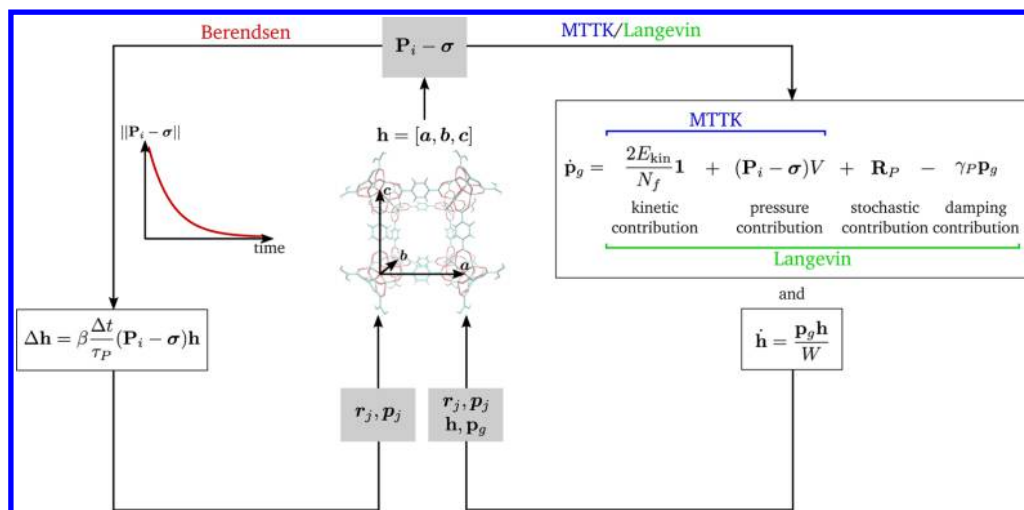


Figure 1. An overview of the different barostats compared in this work and how they handle pressure control via rescaling of the unit cell tensor \mathbf{h} . Some dependencies of the positions and momenta are omitted for clarity, as well as the effect of coupling to a thermostat. In this work, we always assume $\sigma_a = 0$, and thus, $\sigma = P\mathbf{1}$.

frame and are irrelevant for determining the physical properties of the system. Of the remaining six physical degrees of freedom, one is assigned to the volume, whereas the other five are contained in \mathbf{h}_0 and describe the shape of the unit cell.

An analogous separation can be applied to the external stress tensor σ , which is assumed to be symmetric. Indeed, any asymmetry results in a global rotation of the unit cell, and thus yields no additional information. This symmetric tensor with six degrees of freedom consists of a hydrostatic pressure $P = \text{Tr}(\sigma)/3$ and a deviatoric stress σ_a with the remaining five degrees of freedom⁷⁹

$$\sigma = P\mathbf{1} + \sigma_a \quad (2)$$

with $\text{Tr}(\sigma_a) = 0$. It will be shown in the [Methodology](#) section that the isotropic and anisotropic contributions to the stress tensor result in different material responses.

These four thermodynamic quantities— V , \mathbf{h}_0 , P , and σ_a —can be used to define a variety of thermodynamic ensembles. In [Table 1](#), an overview is given of the possible ensembles defined by fixing one or more of these four quantities, as well as the number of particles (N), the total energy (E) or generalized enthalpy (H), and the temperature (T). The ensemble notation as used in common MD packages (DL_POLY,⁸⁰ lammmps,⁸¹ and CP2K⁸²) is shown in the last column of [Table 1](#). These common names are not able to discriminate between all different thermodynamic ensembles. Hence, we need a decomposition of the unit cell and stress tensor into an isotropic and anisotropic part to unequivocally label the ensembles and assign the quantities that are kept constant. In the remainder of this paper, the extended notation that is proposed in the first column of [Table 1](#) will be systematically adopted to avoid confusion.

2.2. Barostats Used to Control the Pressure. For this comparative study, three distinct barostats were considered and implemented in Yaff, our in-house developed software package for MD simulations.⁸³ We explicitly refer to this software package for the implementation, as it was shown that the choice of discretization technique can influence the simulation outcome, even when starting from the same equations of motion.^{84–86} An overview of the investigated barostats is given

in [Figure 1](#) in which the instantaneous pressure tensor \mathbf{P}_i is defined as

$$\mathbf{P}_i = \frac{1}{V} \left[\sum_{j=1}^N \frac{\mathbf{p}_j \otimes \mathbf{p}_j}{m_j} - \Xi \right] \quad (3)$$

where V is the volume occupied by the system consisting of N particles with masses m_j and momenta \mathbf{p}_j , and Ξ is the virial tensor as defined in [section 1](#) of the [Supporting Information](#). The instantaneous (scalar) pressure P_i is found as the average of the diagonal elements of the pressure tensor

$$P_i = \frac{1}{3} \text{Tr}(\mathbf{P}_i) \quad (4)$$

These definitions naturally emerge when considering a Hamiltonian derivation of the equations of motion for a system under conditions of a constant external pressure, as shown in [section 1](#) of the [Supporting Information](#).

The aim of each barostat coupling method is to alter the instantaneous pressure tensor \mathbf{P}_i such that on average the external stress σ is retrieved. Not only does the method to achieve this condition differ for each barostat, but also, with a given barostat implementation, different results can be obtained by tuning the influence of the barostat on the system. This last effect is quantified by the barostat relaxation time τ_P . This input parameter introduces a time scale for the system to respond to an external pressure. Thus, a low barostat relaxation time indicates a very aggressive barostat, which strongly interferes with the dynamics of the system. At the other limit, barostats with a high relaxation time influence the system much less abruptly, and the system will need more time to adapt to a new pressure condition. In the limit for $\tau_P \rightarrow \infty$, no pressure control is present.

The first barostat employed in this study was introduced by Berendsen and co-workers in 1984.¹⁹ In the Berendsen barostat, both the positions \mathbf{r}_j of the particles and the cell tensor \mathbf{h} are rescaled at every integration step with the matrix $\mu = \mathbf{1} + \beta(\mathbf{P}_i - \sigma)\Delta t/\tau_P$, where β is the isothermal compressibility. This step aims at an exponential damping of the difference between the instantaneous internal pressure \mathbf{P}_i and the external stress σ , as is shown in the left branch of [Figure](#)

Table 1. Overview of the Different Thermodynamic Ensembles that can be Considered When Choosing the Fixed Boundary Conditions from the Number of Particles (N), Volume (V), Normalized Unit Cell Tensor (\mathbf{h}_0), Average Hydrostatic Pressure ($\langle P \rangle$), Average Deviatoric Stress ($\langle \sigma_a \rangle$), Generalized Enthalpy (E or H), and Average Temperature ($\langle T \rangle$)^a

ensemble	N	V	\mathbf{h}_0	$\langle P \rangle$	$\langle \sigma_a \rangle$	E or H	$\langle T \rangle$	commonly used notation
$NV(\mathbf{h}_0)E$	×	×	×			×		NVE^{80-82}
$NV(\mathbf{h}_0)T$	×	×	×				×	NVT^{80-82}
$NV(\sigma_a)H$	×	×			×	×		
$NV(\sigma_a)T$	×	×			×		×	
$NP(\mathbf{h}_0)H$	×		×	×		×		$NPH^{80,81}$ NPE_i^{82}
$NP(\mathbf{h}_0)T$	×		×	×			×	$NPT^{80,81}$ NPT_i^{82}
$NP(\sigma_a)H$	×			×	×	×		NPH^{81}
$NP(\sigma_a)T$	×			×	×		×	NPT^{81}
$NV(\sigma_a = 0)H$	×	×			$\langle \sigma_a \rangle = 0$	×		
$NV(\sigma_a = 0)T$	×	×			$\langle \sigma_a \rangle = 0$		×	
$NP(\sigma_a = 0)H$	×			×	$\langle \sigma_a \rangle = 0$	×		$N\sigma H^{80}$ NPE_F^{82}
$NP(\sigma_a = 0)T$	×			×	$\langle \sigma_a \rangle = 0$		×	$N\sigma T^{80}$ NPT_F^{82}

^aFor completeness, ensemble names that are conventionally used in standard MD software packages are included as well. The ensembles for which $\langle \sigma_a \rangle = 0$ are special cases of the more general ensembles defined in the upper part of the table.

1. However, this strong damping of the pressure difference $\mathbf{P}_i - \boldsymbol{\sigma}$ is unphysical and disfavors strong fluctuations in both kinetic and potential energy. Although the Berendsen barostat succeeds in imposing the average hydrostatic pressure P_p , it fails to retrieve the correct fluctuations of this instantaneous pressure, artificially reducing the variance of P_p , as shown below. An analogous technique is used in the Berendsen thermostat, for which it was shown that the resulting temperature distribution deviates from the theoretical distribution.⁸⁷

The second barostat technique in this work is the algorithm proposed by Martyna, Tuckerman, Tobias, and Klein, the MTTK barostat.^{39,40} This method can be seen as the natural extension of the Nosé–Hoover and Nosé–Hoover chain thermostat.^{25,27} In their barostat, a cell momentum tensor \mathbf{p}_g is associated with the unit cell tensor \mathbf{h} and drives the fluctuations of this unit cell tensor. The equations of motion of the cell momentum tensor \mathbf{p}_g depend on both the kinetic energy E_{kin} and the difference between the desired isotropic stress tensor $\boldsymbol{\sigma} = P\mathbf{I}$ and the instantaneous pressure tensor \mathbf{P}_i following

$$\dot{\mathbf{h}} = \frac{\mathbf{p}_g \mathbf{h}}{W} \quad (5a)$$

$$\dot{\mathbf{p}}_g = (\mathbf{P}_i - P\mathbf{I})V + \frac{2E_{\text{kin}}}{N_f} \mathbf{I} - \frac{p_\xi}{Q} \mathbf{p}_g \quad (5b)$$

The barostat mass W ,

$$W = (N_f + 9) \frac{k_B T}{2} \left(\frac{\tau_p}{2\pi} \right)^2 \quad (6)$$

scales as the square of the barostat relaxation time τ_p , and N_f is the number of degrees of freedom in the system. The factor $k_B T$, with k_B Boltzmann's constant, introduces a natural energy scale. The last term in eq 5b stems from the temperature control via a Nosé–Hoover thermostat with mass Q and thermostat momentum p_ξ . These equations of motion are shown in the right branch of Figure 1, where the temperature control term is not displayed for clarity. To be consistent with the required phase space distribution, the cell momentum tensor \mathbf{p}_g should also enter in the equations of motion for the positions \mathbf{r}_j and momenta \mathbf{p}_j of the particles. The proof of the

correctness of this algorithm, which is not straightforward, was carried out by Tuckerman et al. for the case of an isotropic pressure.⁸⁸ Thanks to the deterministic nature of the MTTK barostat, one can theoretically reverse time to propagate the system backwards. Furthermore, this method is characterized by a conserved energy, which proved to be a fast initial verification of the implementation.

The third barostat under consideration is the Langevin piston method,^{9,41} which is based on the Langevin thermostat.¹⁰ As in the MTTK barostat, the unit cell tensor \mathbf{h} has a cell momentum tensor \mathbf{p}_g associated with it. The equations of motion resemble eq 5b, but an additional damping force $-\gamma_p \mathbf{p}_g$ and stochastic force \mathbf{R}_p are introduced:

$$\dot{\mathbf{p}}_g = (\mathbf{P}_i - P\mathbf{I})V + \frac{2E_{\text{kin}}}{N_f} \mathbf{I} - \gamma_p \mathbf{p}_g + \mathbf{R}_p \quad (7)$$

with γ_p the damping coefficient, which is proportional to $1/\tau_p$. The magnitude of \mathbf{R}_p is coupled with γ_p , and hence τ_p , through the fluctuation–dissipation theorem. These two new terms introduce a Brownian motion for the cell momentum tensor. Consequently, the system decorrelates faster in time, but the algorithm is no longer time-reversible. This barostat is represented in the right branch of Figure 1.

Despite their differences, the MTTK and Langevin barostats should yield the correct ensemble in contrast to the Berendsen barostat. To illustrate this, the probability density function (PDF) of the instantaneous pressure P_i in an MD simulation of MIL-53(Al) is examined using the three barostats. The MD simulation is performed in the $(N, P, \sigma_a = 0, T)$ ensemble for $P = 1$ MPa, $T = 300$ K and relaxation times of $\tau_T = 0.1$ ps for the thermostat and $\tau_p = 1.0$ ps for the barostat. The result of this comparison is displayed in the left pane of Figure 2, which shows that the MTTK and Langevin barostats yield the same pressure distribution, whereas the Berendsen barostat clearly disfavors large fluctuations in the internal pressure. Because of the large fluctuations for the MTTK and Langevin barostats, which can be up to 2000 times as large as the average instantaneous pressure $\langle P_i \rangle = 1$ MPa, the mean internal stress converges less quickly to the external stress. This might complicate the equilibration process, which is why the Berendsen barostat is often used during an initial equilibration. Also displayed in the right pane of Figure 2 is the running

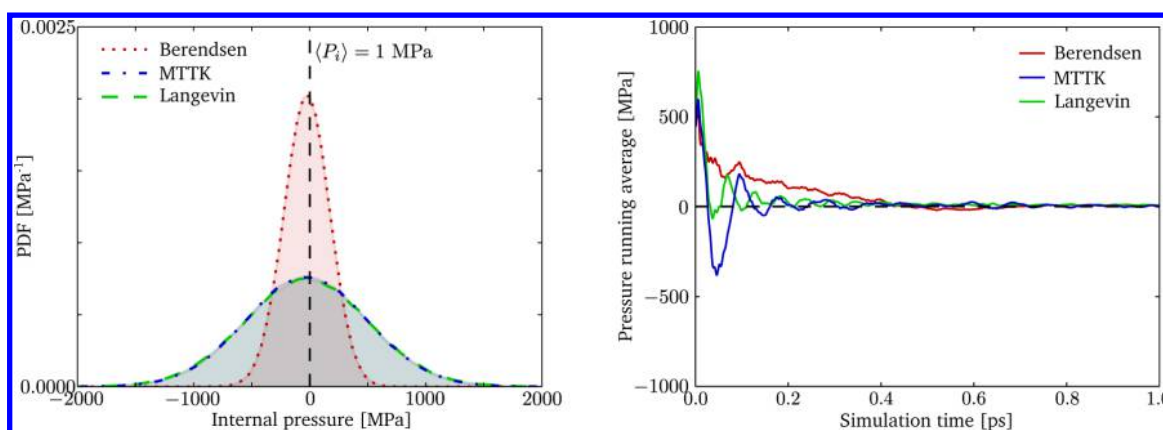


Figure 2. Internal pressure of MIL-53(Al) in an $(N, P, \sigma_a = 0, T)$ simulation (1 MPa, 300 K) using the three barostats under study and starting from the metastable LP structure at 0 K. (left) Probability density function (PDF) generated over a simulation time of 800 ps. (right) Running average of the internal pressure generated for the first picosecond.

average of the instantaneous pressure, defined as the moving average of the instantaneous pressure over the interval $[0, t]$. For all barostats, equilibration takes place within 1 ps, where the Langevin barostat is the fastest for this material.

2.3. Methodology for the Mechanical Characterization of MOFs. As mentioned in the [Introduction](#), various properties will be derived from the MD simulations. For this, two types of ensembles will be used, which are outlined below.

2.3.1. The $(N, P, \sigma_a = 0, T)$ Ensemble for Pressure Responses. To assess the performance of the three barostats under consideration, we carried out MD simulations for the two metal–organic frameworks (MIL-53(Al) and MOF-5) at 300 K and with an isotropic external pressure. These conditions fall under the category of an $(N, P, \sigma_a = 0, T)$ ensemble (see [Table 1](#)). Several simulations have been performed with a pressure between 100 kPa and 1 GPa, starting from the optimized large-pore structure at 0 K for MIL-53(Al) or the global optimized structure at 0 K for MOF-5. For MOF-5, special attention is paid to the stability of the cell parameters and the internal geometry. For MIL-53(Al), it is investigated in which of the two states the system will reside during the simulation: the large pore (LP) or closed pore (CP). The unit cell volume is taken here as criterion: when it crosses a threshold volume V_{tr} , we assume that a transition between the two phases has taken place. For MIL-53(Al), a threshold volume of $V_{tr} = 1000 \text{ \AA}^3$ is chosen based on the volumes of CP and LP structures obtained in earlier works.^{59,65} For further analysis, we also define the time to transition $t_{LP \rightarrow CP}$ as the time needed for the system to undergo this LP-to-CP transition in an MD simulation starting from the LP phase (see [Figure S1](#))

$$t_{LP \rightarrow CP} = \min\{t | V_i(t) \leq V_{tr}\} \quad (8)$$

2.3.2. The $(N, V, \sigma_a = 0, T)$ Ensemble for Thermodynamic Integration. Although the $(N, P, \sigma_a = 0, T)$ ensemble is the most used ensemble to describe materials under constant pressure, a new ensemble will be used to extract the free energy profile and derived properties, such as the transition pressure and bulk modulus. This free energy profile is generated at a finite temperature because it was shown that temperature plays an important role in determining the mechanical properties of MOFs.⁸⁹ For the determination of these mechanical quantities, we propose the use of the $(N, V, \sigma_a = 0, T)$ ensemble. In this ensemble, the volume V and the deviatoric stress σ_a are kept fixed, whereas the cell shape and isotropic instantaneous

pressure are not constrained. In practice, this ensemble can be derived from the MTTK barostat in [eq 5](#). Indeed, the update of the cell volume V and the normalized unit cell tensor \mathbf{h}_0 can be completely separated. Using [eq 1](#), the equations of motion may be rewritten as

$$\dot{V} = \frac{p_g V}{W_1} \quad (9a)$$

$$\dot{p}_g = 3V(P_i - P) + \frac{6E_{kin}}{N_f} - \frac{p_g}{Q} p_g \quad (9b)$$

$$\dot{\mathbf{h}}_0 = \frac{\mathbf{p}_{g,0} \mathbf{h}_0}{W_2} \quad (9c)$$

$$\dot{\mathbf{p}}_{g,0} = V(\mathbf{P}_i - P\mathbf{1}) - \frac{V}{3}\text{Tr}(\mathbf{P}_i - P\mathbf{1})\mathbf{1} - \frac{p_g}{Q}\mathbf{p}_{g,0} \quad (9d)$$

where we replaced the full cell momentum tensor \mathbf{p}_g by a scalar part p_g and a tensorial part $\mathbf{p}_{g,0}$ with $\text{Tr}(\mathbf{p}_{g,0}) = 0$, which are decoupled. Moreover, instead of one barostat mass W in [eq 5a](#), two barostat masses W_1 and W_2 are introduced, which can be chosen independently.

Next, the instantaneous pressure is split into an isotropic and an anisotropic part as $\mathbf{P}_i = P_i \mathbf{1} + \sigma_{i,a}$ similarly to [eq 2](#). [Eq 9d](#) can then be rewritten as

$$\dot{\mathbf{p}}_{g,0} = V\sigma_{i,a} - \frac{V}{3}\text{Tr}(\sigma_{i,a})\mathbf{1} - \frac{p_g}{Q}\mathbf{p}_{g,0} \quad (10)$$

which is completely independent of the isotropic pressure P . Hence, the equation of motion of $\mathbf{p}_{g,0}$, and thus also the equation of motion of the normalized unit cell tensor \mathbf{h}_0 , only depends on the deviatoric internal stress $\sigma_{i,a}$. Finally, we can choose $W_1 \rightarrow \infty$, in which case $\dot{V} = 0$; the cell volume is kept fixed. However, the cell shape can still fluctuate through the second set of equations ([eqs 9c](#) and [9d](#)) because W_2 remains finite. Hence, we finally arrive at the $(N, V, \sigma_a = 0, T)$ ensemble. A similar procedure can be applied for the Berendsen and Langevin barostats such that this new ensemble can be implemented for all three pressure coupling methods.

From the MD simulations in the $(N, V, \sigma_a = 0, T)$ ensemble, the ensemble average of the instantaneous hydrostatic pressure $\langle P_i \rangle$ is measured. Our choice of ensemble ensures that the system can relax its structure under the sole constraint of a

constant volume. Because the hydrostatic pressure is the negative volume derivative of the free energy, one can compute this free energy relative to some reference point via thermodynamic integration:⁹⁰

$$F(V) - F(V_{\text{ref}}) = \int_{V_{\text{ref}}}^V \frac{\partial F(V')}{\partial V'} dV' = - \int_{V_{\text{ref}}}^V \langle P_i(V') \rangle dV' \quad (11)$$

In practice, the integration is carried out by performing $(N, V, \sigma_a = 0, T)$ MD simulations at a series of volumes in a closely spaced volume grid to numerically approximate the integral of eq 11 by a finite sum. In this paper, the initial structures for these $(N, V, \sigma_a = 0, T)$ simulations, which need to have the correct volume V , are taken as snapshots from a regular $(N, P, \sigma_a = 0, T)$ simulation. To generate these snapshots, the $(N, P, \sigma_a = 0, T)$ simulation is started at a sufficiently large volume V_M and a sufficiently high external pressure P , such that the structure will shrink and reach a minimal volume V_m after sweeping through all volumes in $[V_m, V_M]$. If one is interested in an initial structure with unit cell volume $V \in [V_m, V_M]$, a snapshot of the system is taken with a unit cell volume V_i that is the closest to V and differs maximally by 1 \AA^3 for MIL-53(Al) and 2 \AA^3 for MOF-5. Any remaining mismatch between V_i and V is removed by rescaling the unit cell tensor and the coordinates isotropically by a factor $(V/V_i)^{1/3}$. The volume grid spacing is chosen larger than 2 \AA^3 so that two neighboring volume grid points will always start from a different initial configuration.

A series of $(N, V, \sigma_a = 0, T)$ simulations also leads to the determination of the bulk modulus, which gives information about the elasticity of the MOF. Different definitions are used throughout the literature.^{91–93} In this work, the bulk modulus K at a given volume V will be determined based on the monitored $\langle P_i \rangle$ following the relation

$$K(V) = -V \frac{\partial \langle P_i \rangle}{\partial V} \quad (12)$$

Here, $\langle P_i \rangle$ as a function of the volume is first fitted by means of a polynomial so that the integration of eq 11 and the derivative of eq 12 can be carried out analytically, hence reducing the noise. The degree of the polynomial is always odd to correctly describe the asymptotic behavior of the free energy. The maximal polynomial degree is chosen such that no overfitting issues arise, i.e., the Vandermonde matrix corresponding to the fit cannot be rank-deficient.

3. COMPUTATIONAL DETAILS

In this work, all MD simulations are carried out in either the $(N, P, \sigma_a = 0, T)$ or the $(N, V, \sigma_a = 0, T)$ ensemble, in which the number of particles is kept fixed, and the temperature as well as the deviatoric internal stress are controlled. Additionally, in the first ensemble, the average isotropic pressure is imposed to be constant, whereas the volume is kept fixed in the second ensemble. All these simulations are carried out at a temperature of $T = 300 \text{ K}$ using in-house developed force fields that contain covalent, electrostatic, and van der Waals contributions.^{94,95} These force fields have already shown their accuracy to reproduce geometrical properties of the two MOFs, MIL-53(Al) and MOF-5. Further details on the construction of the force fields can be found in refs 94 and 95.

In each of the simulations, the three barostats have been applied in turn and extended with the appropriate thermostat

(Berendsen, Nosé–Hoover, or Langevin thermostat) with a relaxation time of 0.1 ps. (i) The MIL-53(Al) simulations are carried out with a Verlet time step of 0.5 fs for a total simulation time of 800 ps, which turned out to be sufficient for the properties under study. For the barostat, the relaxation time is varied between 1, 5, and 10 ps. A supercell obtained by aligning two unit cells in the direction of the shortest cell vector is considered, which contains a total of 152 atoms. A pressure profile for a supercell containing 304 atoms was also simulated, confirming that increasing the supercell does not appreciably influence the pressure profile. (ii) For MOF-5, the Verlet time step can be increased to 0.75 fs due to the absence of the high-frequency O–H mode, and the total simulation time is 600 ps. Only one unit cell is considered, which already contains 424 atoms. The relaxation time constants are the same as for the MIL-53 simulations. VMD was used to visualize different snapshots of the simulations.⁹⁶

For the initial structure of the $(N, P, \sigma_a = 0, T)$ simulations, the equilibrium state at zero pressure and temperature is taken. The LP state was chosen for MIL-53(Al). For MIL-53(Al), simulations were carried out with a fixed isotropic pressure P between 100 kPa and 1 GPa in nine pressure steps. This broad pressure range is in accordance with the range required to fully characterize the flexible material, as mentioned in the Introduction. For every pressure, 100 simulations were carried out for the MTTK and Langevin barostats. For the Berendsen barostat, 10 simulations proved to be sufficient to accurately determine the time to transition. The structural parameters for the LP phase of this material are averaged over the interval $[0, t_{\text{LP} \rightarrow \text{CP}} - 2\tau_p]$, whereas the CP phase averages are determined based on the interval $[t_{\text{LP} \rightarrow \text{CP}} + 2\tau_p, t_{\text{end}}]$. Here, $t_{\text{LP} \rightarrow \text{CP}}$ is the time to transition of eq 8, and t_{end} denotes the end of the simulation. To gather statistics inherent to the LP and CP states, a time span of $2\tau_p$ before and after the transition is cut out of the trajectory, as shown in Figure S1. For MOF-5, the fixed isotropic pressure for each simulation is chosen between 100 kPa and 30 MPa in six pressure steps. Note that the highest pressures for MIL-53(Al) are not used here because MOF-5 is much more rigid, and less variation in the simulated parameters is expected. To obtain the initial structures for the $(N, V, \sigma_a = 0, T)$ simulations, we followed the procedure as outlined in the Methodology section (section 2.3.2). The computational parameters are unchanged with respect to the $(N, P, \sigma_a = 0, T)$ ensemble simulations. For MOF-5, the unit cell volume takes values in the interval $[16915 \text{ \AA}^3, 18615 \text{ \AA}^3]$ with a step size of 10 \AA^3 , whereas for MIL-53(Al), the unit cell volume is comprised in the interval $[725 \text{ \AA}^3, 1535 \text{ \AA}^3]$ with a step size of 5 \AA^3 .

4. RESULTS AND DISCUSSION

The different barostats and corresponding relaxation times will be tested on a variety of properties. In section 4.1, we will discuss the geometry and stability of the closed-pore (CP) and the large-pore (LP) states of MIL-53(Al) as well as of the equilibrium state of MOF-5. The cell parameters will be determined and compared with experimental values. Moreover, for MIL-53(Al), internal coordinates will be defined that are shown to play an important role in the LP-to-CP transition.⁵⁹ In section 4.2, the free energy profile will be derived for both materials, allowing for an estimation of the bulk moduli and transition pressures. The transition pressures can also be determined directly via a set of $(N, P, \sigma_a = 0, T)$ simulations, which are performed in section 4.3.

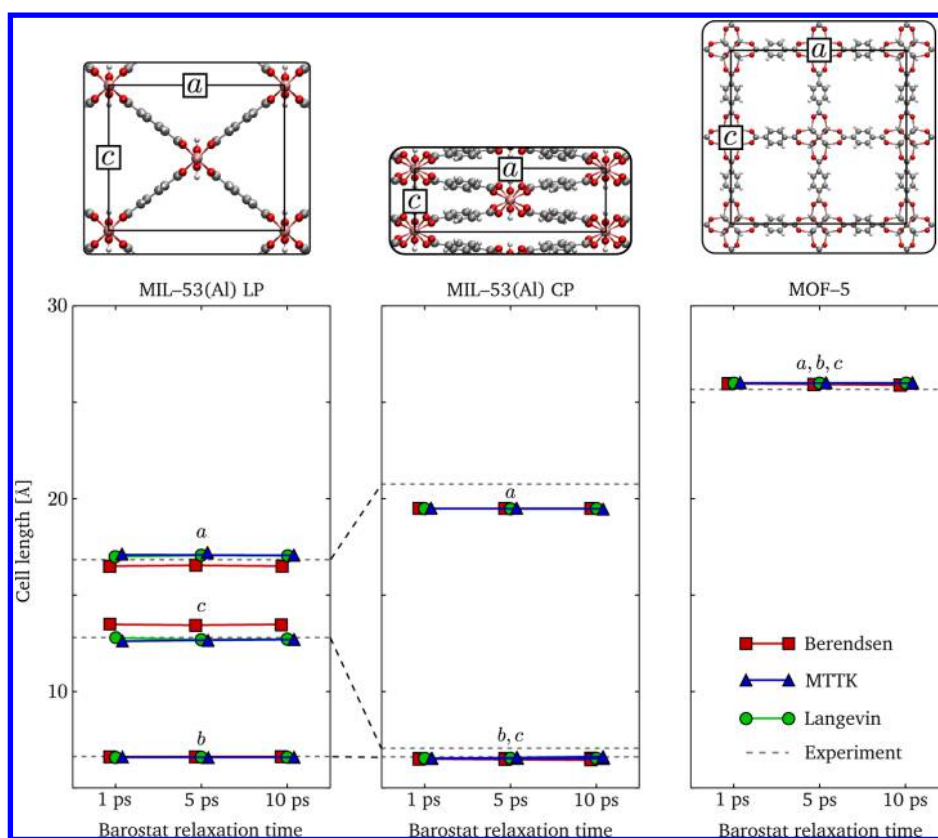


Figure 3. Cell parameters for the LP and CP states of MIL-53(Al) and the stable state of MOF-5 as averages from ten ($N, P, \sigma_a = 0, T$) simulations at 100 kPa and 300 K using the three barostats and for three relaxation times. The b axis of MIL-53(Al) corresponds to the direction of the metal oxide chain, whereas the other cell axes are introduced in the inset. Experimental values (dashed lines) are taken from refs 46 and 65 and carried out at atmospheric pressure. The sampling errors on the cell parameters are very small (<0.3 Å) and tabulated in Tables S1–S3.

4.1. Characterization of the Stable and Metastable States. 4.1.1. Unit Cell Parameters of MIL-53(Al) and MOF-5.

For the characterization of the stable state of MOF-5 and the LP and CP states of MIL-53(Al), ten ($N, P, \sigma_a = 0, T$) simulations are carried out for the three different barostats with various barostat relaxation times τ_p . The resulting cell parameters (see Figure 3) are reported in Tables S1–S3. In the case of MIL-53(Al), the b axis corresponds to the direction of the metal oxide chain. The MD simulations are carried out at 300 K and at different pressures varying between 100 kPa and 1 GPa. For each of the data points, the sampling error is calculated as the standard deviation for the ten simulations, which are assumed to be independent by choosing different initial conditions. The sampling errors are smaller than 0.3 Å and are given in Tables S1–S3.

Figure 3 illustrates how the simulation results are hardly affected by the barostat relaxation time at 100 kPa but are sensitive to the choice of the barostat. In all cases, the MTTK and Langevin results are comparable, whereas the Berendsen barostat deviates slightly in the particular case of MIL-53(Al) LP. The estimates of the a and c cell lengths differ from the other two barostats, as seen in Table S1. The discrepancy amounts to a value of approximately 0.5–1.0 Å and turns out to be three times larger than the largest standard deviation. These directions are the most flexible in the LP structure of MIL-53(Al), as was determined earlier by Ortiz et al.⁹⁷

Moreover, as shown in section 2.3 of the Supporting Information, both unit cell vectors are strongly coupled. A scatter plot of the cell lengths a and c in the LP phase during an

($N, P, \sigma_a = 0, T$) simulation shows that the free energy minimum area in the (a, c) plane, determined by the most frequently visited configurations, is characterized by an elongated, narrow region when using the MTTK and Langevin barostats (Figure S3). Because of the reduced pressure fluctuations, the Berendsen barostat converges only very slowly, explaining the observed difference in the predicted cell lengths for these soft directions. Increasing the simulation time for the Berendsen barostat, however, does not yield an appropriate alternative due to other well-known artifacts of that barostat.^{5,6}

($N, P, \sigma_a = 0, T$) MD simulations at higher pressures, up to 1 GPa, were also carried out, leading to the same conclusions regarding the performance of the barostat and barostat relaxation time.

All cell lengths of the MIL-53(Al) LP and MOF-5 equilibrium structure simulated with the MTTK and Langevin barostats coincide fairly well with the experimental estimates. In particular, these ($N, P, \sigma_a = 0, T$) simulations confirm the cubic structure (space group $Fm\bar{3}m$) of MOF-5⁴⁶ and yield the space group $Pmma$ for the LP structure and $P2_1/c$ for the CP structure of MIL-53(Al). These symmetry groups correspond to those found experimentally when correcting for the fact that the simulated BDC linkers have a small and opposite tilting, which is not easy to observe via XRD due to the small reflectance of the carbon atoms and the associated large error on their positions.⁶⁵ For the reproduction of the CP structure in MIL-53(Al), some deviation from experimental values is noticed, but this is probably due to a force-field effect, as has been reported earlier.⁹⁴ A similar analysis, carried out for the cell angles α, β ,

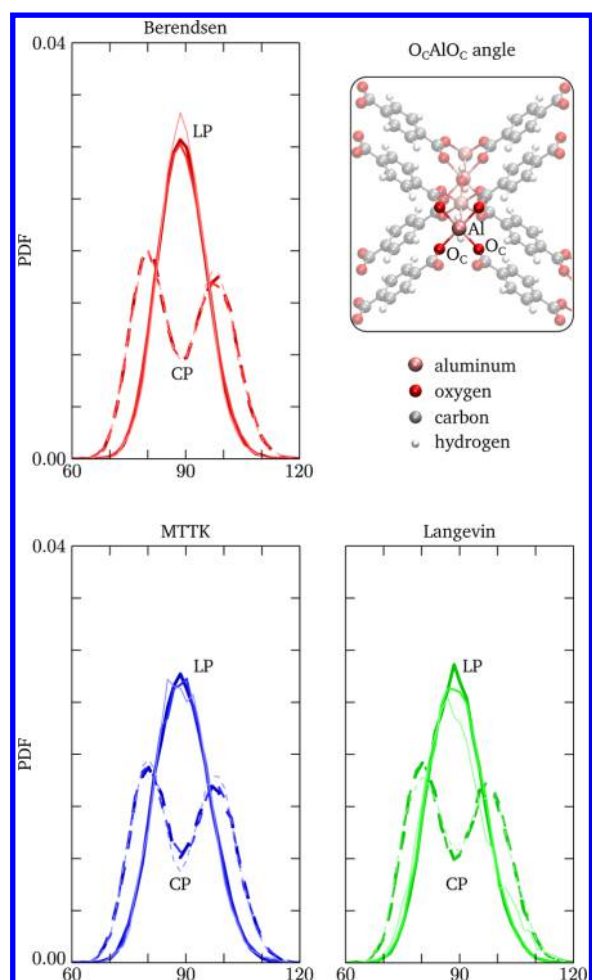


Figure 4. Probability density function (PDF, in $1/^\circ$) of the O_CAlO_C angles (in $^\circ$) present in the unit cell of MIL-53(Al) in both the large-pore (full line) and the closed-pore (dashed line) structure at 300 K and 1 MPa using the three barostats and barostat relaxation times as indicated in the text. The darker the color, the higher the barostat relaxation time $\tau_p \in [1 \text{ ps}, 5 \text{ ps}, 10 \text{ ps}]$.

and γ , reveals that there is much less spread between the different barostats and barostat relaxation times, as shown in Tables S1–S3. As a consequence, the unit cell volume of the MIL-53(Al) LP phase is slightly overestimated by the Berendsen barostat ($\sim 1470 \text{ \AA}^3$) but is in agreement with experimental values for the MTTK and Langevin barostats ($1415\text{--}1430 \text{ \AA}^3$). The predicted volumes for the stable phases, $814\text{--}834 \text{ \AA}^3$ for the CP phase of MIL-53(Al) and $17364\text{--}17571 \text{ \AA}^3$ for MOF-5, coincide for all barostats.

4.1.2. Internal Coordinates Characterizing the LP \rightarrow CP Transition in MIL-53(Al). Aside from the cell parameters, which give an indication of the collective motion of the atoms, the LP-to-CP transition in MIL-53(Al) can also be characterized by the internal movement of a small, well-chosen set of atoms. In particular, two motions seem predominant in this transition: the O_CAlO_C angle and the AlO_CCC dihedral. The O_CAlO_C angle, shown in Figure 4, is the internal angle between the carboxylate oxygen–aluminum bonds of each of the four linkers. For each aluminum atom, there are thus four such angles exhibiting a magnitude around 90° in the LP phase. The AlO_CCC dihedral, shown in Figure 5, indicates a rotation of the phenyl linker with respect to the metal center about the O–O axis, which was found to act as a kneecap during the LP-to-CP

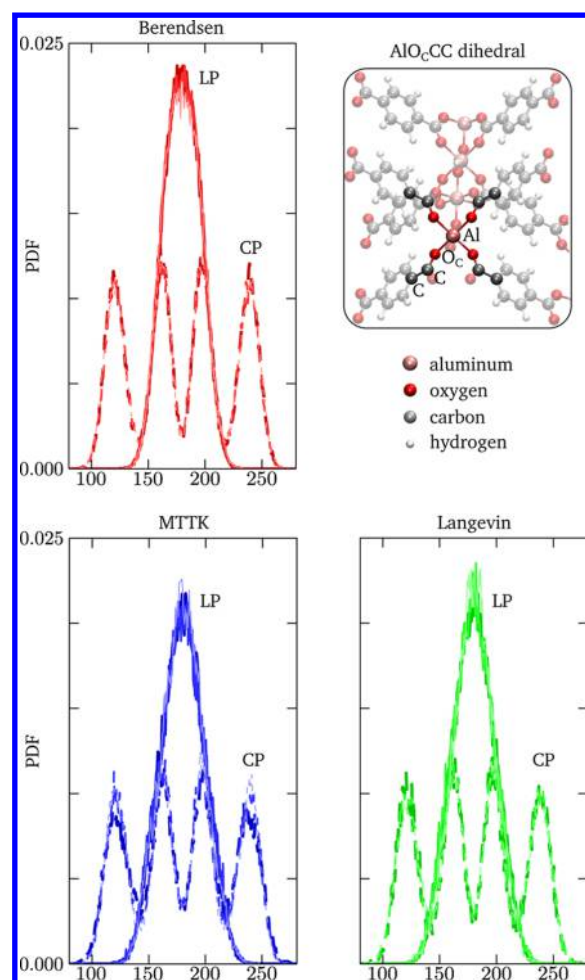


Figure 5. Probability density function (PDF, in $1/^\circ$) of the AlO_CCC dihedral angles (in $^\circ$) present in the unit cell of MIL-53(Al) in both the large-pore (full line) and the closed-pore (dashed line) structure at 300 K and 1 MPa using the three barostats and barostat relaxation times as indicated in the text. The darker the color, the higher the barostat relaxation time $\tau_p \in [1 \text{ ps}, 5 \text{ ps}, 10 \text{ ps}]$.

transition.⁹⁸ Again, four such angles are found for each metal center. For this torsion angle, the IUPAC convention is used,⁹⁹ where the negative angles, in the range $[-180^\circ, 0^\circ]$, were translated to the interval $[180^\circ, 360^\circ]$, enabling a better visualization of the results.

To investigate the change of these internal coordinates, we carried out $(N, P, \sigma_a = 0, T)$ simulations at 300 K and a hydrostatic pressure of 1 MPa. For the MTTK and Langevin barostats, one simulation starting at the LP structure was sufficient to sample both the large pore and the closed pore extensively because a transition to the CP structure was found about midway through the simulations (see, for instance, Figure S1). For the Berendsen barostat, two simulations were carried out per relaxation time: one starting in the LP and one in the CP structure because no LP-to-CP transition occurs at a pressure of 1 MPa.

For the O_CAlO_C angle, we deduce from Figure 4 that the LP-to-CP transition splits the 90° peak into two peaks, at 80° and 100° , separated by a valley in the probability density around 90° . This indicates that, upon transition to the CP structure, two of the phenyl linkers approach each other, decreasing their internal angle by 10° . This behavior is retrieved for each of the

barostats and barostat relaxation times with small deviations for the Berendsen barostat in the LP phase.

The AlO_6CC dihedral (Figure 5) also undergoes a distinct transformation during the LP-to-CP transition. Although this torsion angle is peaked around 180° in the LP structure, the CP distribution function is dominated by four equidistant and equiprobable peaks centered around 120° , 160° , 200° , and 240° . This result shows symmetry with respect to 180° , as expected, and is in agreement with what has been reported in recent work by Yot et al.⁵⁹ This splitting at the CP phase is independent of the barostat and barostat relaxation time. However, the LP peak is slightly narrower when using the Berendsen barostat, confirming once again that the Berendsen barostat does not exactly reproduce the results from the MTTK and Langevin barostats in the LP structure.

4.2. Free Energy Landscapes. Following the method outlined in the Methodology section, $(N, V, \sigma_a = 0, T)$ simulations can be used to generate pressure and free energy profiles as a function of the unit cell volume for MIL-53(Al) and MOF-5. In section 3.4 of the Supporting Information, we also included the free enthalpy profiles at different pressures, yielding an alternative method to follow the discussion below. From these profiles, one can deduce the stable and metastable states as well as the transition pressures and bulk moduli. For all simulations reported in this section, the first 100 ps of the trajectories are regarded as an equilibration period, and properties are derived from the remaining 700 ps (MIL-53(Al)) or 500 ps (MOF-5).

4.2.1. Transition Pressure for MIL-53(Al). As was outlined previously, the $(N, V, \sigma_a = 0, T)$ simulations allow for the determination of the average internal pressure $\langle P_i \rangle$, which is exerted by the material on its environment, as a function of the unit cell volume V . Subsequently, an 11th-order polynomial $\langle P_i(V) \rangle$ is fitted to these results for MIL-53(Al) (see Table S4). The simulations are performed for the three barostats and at three relaxation times τ_p : 1, 5, and 10 ps. The $P_i(V)$ profiles are displayed in the upper pane of Figure 6.

All three barostats yield profiles that almost coincide with each other and that are independent of the chosen relaxation time within the sampling error. The pressure profile in the upper pane of Figure 6 also reveals the stable, and possibly metastable, structure(s) found at a given external pressure. The experimental measurements of the two phases in MIL-53(Al) took place at an external pressure of 100 kPa. According to our profile, three structures correspond to an external pressure of 100 kPa: the CP phase at V_{CP} , the LP phase at V_{LP} , and a transition point situated at V_{tr} that is unstable due to the positive derivative $\partial P/\partial V$. In section 3.4 of the Supporting Information, it is explicitly shown via a committor analysis that this unstable point indeed corresponds to a transition state.^{100,101} The cell parameters of the transition state are given by $a = 18.3 \text{ \AA}$, $b = 6.5 \text{ \AA}$, and $c = 10.7 \text{ \AA}$ and are thus between the CP and LP states.

This pressure profile also predicts how the structures evolve when decreasing or increasing the external pressure because in equilibrium the internal pressure equals the external pressure. The $P_i(V)$ graph shows two extrema: a minimum at $P_{\text{CP} \rightarrow \text{LP}}$ and a maximum at $P_{\text{LP} \rightarrow \text{CP}}$. Between these two pressures, one always encounters three structures (a transition state, a metastable, and a stable state, as is clear from the free enthalpy profiles for these pressures, see Figure S6). For pressures above $P_{\text{LP} \rightarrow \text{CP}}$, only one stable state exists with a volume close to V_{CP} . In this pressure regime, the system remains in the closed pore, and the free

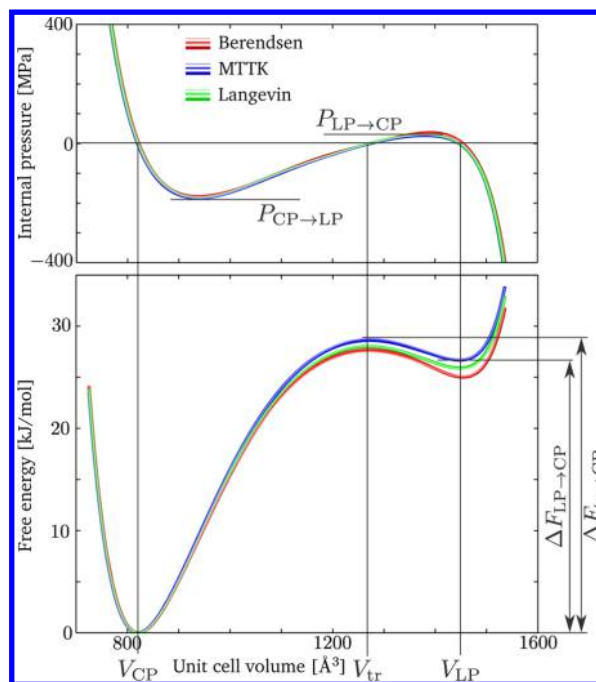


Figure 6. Fitted internal pressure P_i (top) and free energy F (bottom) profiles as a function of the constrained unit cell volume V for MIL-53(Al), resulting from $(N, V, \sigma_a = 0, T)$ simulations at $T = 300 \text{ K}$. For each barostat, three barostat relaxation times τ_p were considered: 1, 5, and 10 ps, where the color of the graph is darker the higher the relaxation time. For all barostats, the graphs coincide within the average error of the order of 1 MPa on the $P_i(V)$ plot and 0.05 kJ/mol on the $F(V)$ plot, as calculated via a bootstrap procedure (see the Supporting Information). Simulated values of the equilibrium volumes, transition pressures, energy differences, and bulk moduli are tabulated in Table S6.

enthalpy profile of Figure S6 indeed reveals only one minimum. Similarly, the system remains in the large pore for pressures below $P_{\text{CP} \rightarrow \text{LP}}$. An overview of the simulated values for the aforementioned volumes and transition pressures is reported in Table S6.

In summary, when starting from MIL-53(Al) in the LP phase at a pressure for which this phase is either stable or metastable, the volume of the material will systematically decrease with increasing pressure. Once the pressure reaches $P_{\text{LP} \rightarrow \text{CP}}$, the structure goes over from the metastable LP to the stable CP phase with a volume reduction of $\sim 35\%$ because the LP minimum in the free enthalpy disappears (see Figure S6). The material remains in this phase when further increasing the pressure. In section 4.3, it will be discussed how fast this transition takes place. The reverse transformation occurs when starting from a CP structure at high pressures, for which it is again either stable or metastable. When systematically decreasing the external pressure, the material transforms from the metastable CP into the stable LP structure once the pressure reaches $P_{\text{CP} \rightarrow \text{LP}}$, corresponding to the disappearance of the free enthalpy minimum. Hence, for an external pressure between these two transition pressures, the two phases may coexist as a stable and a metastable phase, and the phase observed during an experiment depends on the prior external conditions.⁵⁹ The pressure profile thus indicates the existence of a hysteresis curve if negative pressures can be achieved experimentally. Negative pressures correspond to pulling the material isotropically and may occur, for instance, when this

MOF is embedded in a polymer film. More information on the occurrence of a particular phase and the transition among the various phases can be found in a recent paper by Vanduyfhuys et al., where a thermodynamic model was proposed to predict the conditions for phase transitions of flexible materials.^{102,103}

The transition pressure $P_{\text{CP} \rightarrow \text{LP}}$ varies between -183 and -177 MPa irrespective of the choice of barostat, whereas $P_{\text{LP} \rightarrow \text{CP}}$ varies between 27 and 30 MPa using the MTTK and Langevin barostats. These results for $P_{\text{LP} \rightarrow \text{CP}}$ are in good agreement with the experimental values of 13–18 MPa at 300 K.⁵⁹ The Berendsen barostat predicts a transition pressure $P_{\text{LP} \rightarrow \text{CP}}$ between 33 and 38 MPa, which deviates slightly from the results obtained with the other two barostats. This observation is in line with the results depicted in Figures 3–5, where only in the LP phase some deviation from the other two barostats is present. Note that the transition volume V_{tr} is $\sim 1270 \text{ \AA}^3$ instead of the ad hoc introduced value of 1000 \AA^3 in eq 8. However, replacing this ad hoc value by the proper value of 1270 \AA^3 to distinguish between the LP and CP phases does not significantly alter the time to transition $t_{\text{LP} \rightarrow \text{CP}}$ because the time the system spends in the transition region is small compared to the time spent in the (meta)stable states (see Figure S1).

4.2.2. Free Energy Landscapes and Bulk Moduli for MIL-53(Al) and MOF-5. By integrating the pressure profile according to eq 11, the free energy profiles for MIL-53(Al) and MOF-5, which are shown in Figure 6 (bottom) and Figure 7, are retrieved. For this integration, the CP volume is chosen

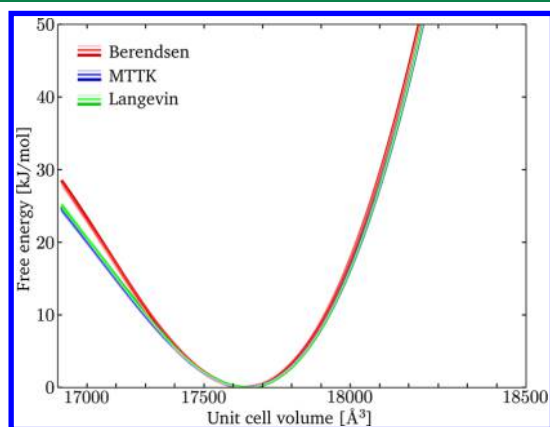


Figure 7. Free energy F as a function of the constrained unit cell volume V for MOF-5, resulting from $(N, V, \sigma_a = 0, T)$ simulations at $T = 300$ K. For each barostat, three barostat relaxation times τ_p were considered: 1, 5, and 10 ps, where the color of the graph is darker the higher the relaxation time. The error on the free energy is on the order of 0.02 kJ/mol, as calculated via a bootstrap procedure (see Supporting Information). Simulated values of the equilibrium volume and bulk modulus are tabulated in Table S7.

as the reference volume for MIL-53(Al), whereas the equilibrium volume of MOF-5 is taken as the reference volume for this material.

The free energy profile of MIL-53(Al), displayed in the bottom pane of Figure 6, shows two minima corresponding to the closed-pore volume V_{CP} and the large-pore volume V_{LP} . The transition from the LP to the CP structure is slightly activated, prohibiting the LP structure from shrinking to the more deeply bound CP structure without external stimuli. Again, it is seen that the choice of the barostat relaxation time does not influence the free energy profile. A free energy

difference between the CP and the LP states of 27.6–28.8 kJ/mol is predicted, and the barrier height amounts to 2.0–3.2 kJ/mol (with respect to the LP structure), depending on the barostat relaxation time. To the best of our knowledge, no experimental information is available on the free energy difference between these two phases, and only recently has the internal energy difference been accessed experimentally.¹⁰⁴ For MOF-5, as shown in Figure 7, similar conclusions can be drawn, where it is observed that all barostats nearly coincide within the given sampling error of 0.02 kJ/mol. For this material, a fifth-order polynomial fit of $\langle P_i \rangle$ as a function of V was carried out (see Table S5).

As indicated in eq 12, the bulk modulus can be calculated based on the internal pressure profile. This calculation is carried out for the equilibrium structure of MOF-5 and the CP and LP states of MIL-53(Al) at 300 K and tabulated in Tables S6 and S7. For MOF-5, bulk moduli of 6.6 to 7.3 GPa are found. These values compare well with earlier simulations, where bulk moduli in the range of 14.4 to 20.0 GPa are reported near or at 0 K.^{68,77,105–111} Force-field simulations further show that the MOF-5 bulk modulus systematically decreases with increasing temperature, reducing to 4.0–16.66 GPa at 300 K.^{108,109} For MIL-53(Al), the bulk modulus of the CP structure amounts to 3.33–3.66 GPa, whereas the LP structure yields a lower bulk modulus of 1.58–2.58 GPa, both calculated using the three barostats with different relaxation times. The lower bulk modulus for the LP structure confirms the intuition that the open structure is more easily compressed than the CP structure. Experimentally, a bulk modulus of 0.35 GPa for the LP phase at 300 K was reported by Yot et al.⁵⁹ Ongoing experiments in this research group indicate a CP bulk modulus of ~ 10 GPa at 300 K.

When comparing the pressure distributions imposed by the different barostats in Figure 2, it was observed that the Berendsen barostat suppresses pressure fluctuations and thus is unable to exactly sample the isobaric ensembles. As shown in Figure S4, this leads to $(N, V, \sigma_a = 0, T)$ simulations for which the Berendsen distribution of the cell parameters is much narrower than the MTTK and Langevin distributions, similar to the pressure and volume distributions during $(N, P, \sigma_a = 0, T)$ simulations (see Figure 2). However, in the preceding discussion, the results obtained with the Berendsen barostat seem to agree well with the MTTK and Langevin results. This rather surprising result is explained based on the linear behavior of the internal pressure as a function of the cell parameters, as shown in Figure S5. Because of this linearity, any symmetric distribution of the cell parameters with the correct mean will result in the same average internal pressure, explaining the coinciding results in Figures 6 and 7. However, it is expected that the Berendsen results will vary appreciably when the properties of interest no longer vary linearly. For instance, an alternative way to calculate the bulk modulus of a material is based on the formula⁹³

$$K = k_B \langle T \rangle \frac{\langle V \rangle}{\langle V^2 \rangle - \langle V \rangle^2} \quad (13)$$

For MIL-53(Al), this bulk modulus is calculated based on the $(N, P, \sigma_a = 0, T)$ trajectories used to determine the distribution of the internal coordinates. Both the MTTK and Langevin barostats predict bulk moduli of 8.5–12.1 GPa (CP) and 3.2–10.1 GPa (LP) at 300 K. These bulk moduli are in agreement with the results obtained based on the pressure profile.

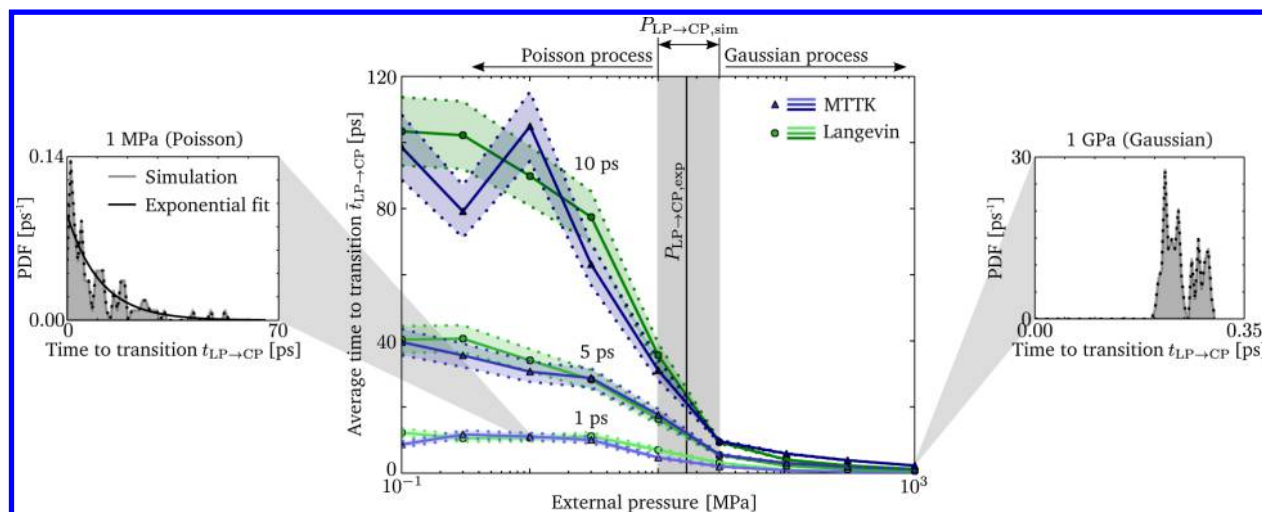


Figure 8. Average simulation time needed to observe the MIL-53(Al) LP-to-CP transition in an $(N, P, \sigma_a = 0, T)$ ensemble at 300 K as a function of the applied pressure and carried out for different barostats and barostat relaxation times of 1, 5, and 10 ps. The shaded regions indicate the 1σ confidence interval for this average simulation time (see Appendix A and Supporting Information). Also indicated are the experimental transition pressure $P_{\text{LP} \rightarrow \text{CP}, \text{exp}}$ and the transition region $P_{\text{LP} \rightarrow \text{CP}, \text{sim}}$ predicted via our statistical analysis. In the side panes, the probability density function (PDF) for the time to transition is displayed for two selected pressures and consists of 100 independent simulation results carried out with the MTTK barostat and a relaxation time of 1 ps. Other pressures are shown in Figure S9.

However, when using the Berendsen barostat, much higher bulk moduli are predicted, amounting to 275–1150 GPa (CP) and 93–215 GPa (LP). These Berendsen results are one to two orders of magnitude higher than the results obtained with the other barostats because the calculation of the bulk modulus explicitly depends on the volume fluctuations.

4.3. Determination of the Transition Pressure and Time to Transition for MIL-53(Al). In the method outlined above, the transition pressure for MIL-53(Al) could be determined from the construction of a P_i versus V profile from a series of $(N, V, \sigma_a = 0, T)$ simulations at different volumes. One can argue that one straightforward $(N, P, \sigma_a = 0, T)$ simulation for a small set of pressures P will reveal the same information, while fewer simulations are needed. The idea is that, when we perform a simulation at a given pressure P and observe the system shrink from the LP to the CP structure, we assume that the pressure P of the simulation is higher than the mechanically required transition pressure $P_{\text{LP} \rightarrow \text{CP}}$. In contrast, if no transition is observed, it is assumed that the pressure P of the simulation is lower than the transition pressure $P_{\text{LP} \rightarrow \text{CP}}$. As such, one can, in principle, easily determine the transition pressure $P_{\text{LP} \rightarrow \text{CP}}$ by choosing a small set of well-chosen pressures. Moreover, this method would also allow us to determine the time $t_{\text{LP} \rightarrow \text{CP}}$ the system needs to undergo this transition (eq 8). This could reveal new insights into the transition process because, to date, no experimental tools are able to capture this transition time as it occurs too fast.¹¹²

For the Berendsen barostat, we observe that the occurrence of a LP-to-CP transition within the simulation time of 800 ps at a certain pressure depends on the barostat relaxation time. For $\tau_p = 1$ ps, a pressure of 30 MPa suffices to steer the structure from the metastable large pore to the stable closed pore. Upon increasing this relaxation time to 5 ps, a pressure of 1 GPa is needed, whereas no transition is seen for $P \leq 1$ GPa when using a relaxation time of 10 ps. Doubling the simulation time to 1.6 ns did not alter these findings. Although the first result is in agreement with experimental observations predicting a transition pressure of 13–18 MPa,⁵⁹ it is clear that the dependence on relaxation time is unphysical and should be

avoided. For the MTTK and Langevin barostat, the time to transition $\bar{t}_{\text{LP} \rightarrow \text{CP}}$, averaged over 100 simulations, shows a completely different behavior, as can be seen in the central pane of Figure 8. A LP-to-CP transition is observed for all pressures, including the low pressures to the left of the vertical line $P_{\text{LP} \rightarrow \text{CP}, \text{exp}}$ in this figure, in contrast to the experimental observations. Moreover, we observe that the average time to transition $\bar{t}_{\text{LP} \rightarrow \text{CP}}$ clearly increases when increasing the barostat relaxation time. This effect is not completely unexpected: the barostat relaxation time τ_p determines how fast the unit cell tensor \mathbf{h} , and hence the volume V , can respond upon external pressure stimuli and will thus regulate the time it takes for the metastable or unstable LP structure to shrink to the stable CP phase. These results indicate that the barostat coupling method cannot be used to determine dynamic variables directly related to the movement of the unit cell tensor as a whole, such as this average time to transition, because it depends on the chosen barostat relaxation time. Note that these average times to transition are relatively fast, independent of the relaxation time, supporting our choice to limit the total simulation time to 800 ps.

However, in section 4.2, we succeeded in determining the transition pressure, a static variable, from the free energy profile. The same information should be present in this dynamic characterization, albeit possibly overshadowed by the interference of the barostats. To extract this information, we will rely on a statistical model to describe the transition, as outlined in Appendix A. For every given choice of barostat, barostat relaxation time, and pressure, we determine whether the simulated time to transition can best be described using a Poisson model, mimicking rare events, or using a Gaussian model, corresponding to a spontaneous transition. We introduce the ratio R as the ratio of the likelihood that the process can be described by a Gaussian or a Poisson model.

If we apply a large external pressure P , higher than the transition pressure, we expect that the system immediately adapts to this pressure and shrinks early in the simulation to the CP phase (low $t_{\text{LP} \rightarrow \text{CP}}$). The only variation in this time to

transition is due to different initial conditions so that we can describe these high-pressure transitions as a Gaussian process. Furthermore, an increase in the applied pressure will increase the steering force, and hence decrease the observed time to transition. This is indeed observed in the high-pressure regime of Figure 8, extending from ~ 30 MPa, where the transition can be described by a Gaussian process and is thus spontaneously occurring at these pressures. Also, the large ratio $R \sim \exp(100)$ in Figure S8 is evidence of this observation.

In contrast, if we apply an external pressure P much lower than the transition pressure, a LP-to-CP transition is not expected. However, we still observe a phase transformation during an $(N, P, \sigma_a = 0, T)$ MD simulation at times much larger than in the high-pressure regime. The large pressure fluctuations when using the Langevin and MTTK barostats, as observed in the left pane of Figure 2, cause this behavior. It is expected that, at a certain point during the simulation, a sequence of pressure fluctuations will appear that have a sufficiently high positive amplitude to drive a LP-to-CP transition. This process yields a much larger time to transition because such a prolonged large pressure fluctuation is an infrequent event, consistent with a Poisson process. However, if the simulation time is sufficiently long, as is the case here, the LP-to-CP transition will certainly take place. As an example, we refer to Figure S1 in which the MIL-53(Al) unit cell volume is shown during an $(N, P, \sigma_a = 0, T)$ simulation at 300 K and at a pressure of 1 MPa, which is lower than the LP-to-CP transition pressure. For the particular simulation displayed in Figure S1, the time to transition $t_{\text{LP} \rightarrow \text{CP}}$ takes place at ~ 320 ps. This whole reasoning is built upon sufficiently large pressure amplitudes, which for a given force field, can depend on the size of the simulation cell and the barostat properties. The experiment is not able to elucidate this process because it occurs too fast.¹¹²

Moreover, because the pressure fluctuations at 300 K and at low pressures are dominated by temperature effects, these transitions are expected to be quasi independent of the applied external pressure, resulting in $\bar{t}_{\text{LP} \rightarrow \text{CP}}$ being fairly independent of P . This low-pressure behavior is indeed observed in Figure 8, up to a pressure of ~ 10 MPa. Furthermore, Figure S8 also reveals that the ratio $R \sim \exp(-80)$ in this pressure range, indicating a clear preference for the Poisson model. Moreover, these results are the same for the MTTK and Langevin barostats and almost independent of the barostat relaxation time. When using the Berendsen barostat, pressure fluctuations are suppressed, so that this LP-to-CP transition will rarely occur within a feasible simulation time, as is indeed observed in our simulations.

In summary, the $(N, P, \sigma_a = 0, T)$ simulations allow for the determination of the LP-to-CP transition pressure (10–30 MPa) but fail to determine dynamic quantities that are directly related to cell fluctuations, as the system is perturbed by the barostat. Not only is this method less accurate than the $(N, V, \sigma_a = 0, T)$ simulations in section 4.2, it is also less efficient. For the $(N, P, \sigma_a = 0, T)$ simulations, a lot of trajectories (here: 100) are needed for every pressure to obtain reliable statistics, whereas for the $(N, V, \sigma_a = 0, T)$ simulations, a few trajectories per volume grid point suffice to determine the $P_i(V)$ profile and its error.

5. CONCLUSIONS

In this work, we have compared three different barostat implementations, the Berendsen, MTTK, and Langevin barostats, to predict static and dynamic properties of metal–

organic frameworks. Whereas the MTTK and Langevin pressure control schemes only differ by the introduction of a Brownian motion in the Langevin scheme, the Berendsen update scheme is completely different. The latter aims at an exponential damping of the difference between the instantaneous and externally applied pressure, hence disfavoring pressure fluctuations. As expected, this results in a pressure distribution that is much narrower than when using the MTTK or Langevin barostat, in agreement with earlier results for the Berendsen thermostat⁸⁷ and barostat.⁹

The effect of the barostat choice has been investigated with $(N, V, \sigma_a = 0, T)$ and $(N, P, \sigma_a = 0, T)$ MD simulations for two materials: the rigid MOF-5 and the flexible MIL-53(Al). First of all, for the large pore of MIL-53(Al), some of the cell length predictions of the Berendsen barostat differ slightly from the MTTK/Langevin and experimental results, even when taking into account the sampling error. Similar minor differences are seen for the internal coordinates playing a dominant role in the MIL-53(Al) LP-to-CP transition. Changing the barostat relaxation time does not appreciably influence these findings.

Second, a thermodynamic integration procedure was applied to derive the free energy as a function of volume for both MIL-53(Al) and MOF-5 at 300 K. Here, the results obtained with the three barostats coincide independent of the barostat relaxation time. This is not in disagreement with the deviating cell shape distribution of the Berendsen barostat due to the linear behavior of the pressure as a function of the cell shape. However, for nonlinear functions, such as those used when calculating the bulk modulus based on the standard deviation of the volume fluctuations, the Berendsen results deviate. From the pressure versus volume curves, the transition pressures from the LP to the CP phase and vice versa are deduced. The experimental LP-to-CP transition pressure is 13–18 MPa at 300 K, which corresponds fairly well to the transition pressures derived from our simulations using the three barostats. Only the Berendsen barostat shows some small deviations.

Third, we have investigated the transition pressures and the time to transition from the $(N, P, \sigma_a = 0, T)$ simulations for MIL-53(Al). The time to shrink from the LP to the CP phase strongly depends on the barostat relaxation time, indicating that a barostat cannot be used to obtain dynamic parameters directly influenced by the cell movement. Nevertheless, we have been able to successfully derive the transition pressure from this type of simulation. For this, we have proposed a statistical criterion to distinguish between a Poisson-type transition (rare event) and a Gaussian-type transition (spontaneous event). For the LP-to-CP transition, the Poisson process is dominant for pressures lower than 10 MPa, whereas the Gaussian process dominates for pressures higher than 30 MPa, yielding a transition range of 10–30 MPa, which is in line with the experimental results. However, this method is less exact than thermodynamic integration and would require more independent simulations to obtain the same accuracy.

In summary, although the Berendsen barostat can be efficiently used to equilibrate a system, it was shown that it should be used with caution when one wishes to obtain accurate results from MD simulations, especially when considering flexible materials. Moreover, we observed that both the MTTK and Langevin barostats yield the same results and are in agreement with experimental results for the calculation of static variables. Thus, the choice between the MTTK and Langevin barostat is a matter of taste or necessity; for instance, only MTTK can be used when one needs to

integrate the equations of motion backward, e.g., as needed for transition path sampling.

Appendix A. Statistical Modeling of the LP-to-CP Transition

In this appendix, we will show how it is possible to classify the observed transitions from the large pore (LP) to the closed pore (CP) in MIL-53(Al) in either Gaussian- or Poisson-like processes based on statistical considerations. For this, consider a simulation in which a LP-to-CP transition is observed after a given time to transition $t_{LP \rightarrow CP}$, as defined in eq 8. This time to transition potentially depends on the applied pressure, the type of barostat, and the barostat relaxation time used to control this pressure. When comparing different simulations with the same barostat properties, it is observed that this time to transition $t_{LP \rightarrow CP}$ does not take a well-defined value for all simulations, but rather follows an underlying distribution defined by the process inducing the transition.

The first statistical model describes these LP-to-CP transitions as uncorrelated occurrences with a very low probability, so-called rare events. The transition can then be modelled as a Poisson process, and the corresponding time to transition is exponentially distributed. This distribution is completely defined by only one parameter t_0 , the decay constant. In the Supporting Information, the estimator t_0^* is introduced as the value of t_0 that maximizes the likelihood of the distribution,^{113,114} which can be seen as the best estimator for t_0 . As outlined in the Supporting Information, the 1σ confidence interval of t_0^* , given the uncorrelated data $X = \{X_1, \dots, X_N\}$ consisting of N observations, is

$$t_0^* = \bar{X} \pm \frac{\bar{X}}{\sqrt{N}} \quad (14)$$

where \bar{X} denotes the sample mean.

In the second statistical model, the LP-to-CP transition is seen as a spontaneous event, and the corresponding times to transition are assumed to be distributed according to the Gaussian distribution, characterized by its mean μ and standard deviation σ . As outlined in the Supporting Information, the 1σ confidence intervals for these estimators are given by

$$\mu^* = \bar{X} \pm \sqrt{\frac{s_X^2}{N-1}} \quad (15)$$

and

$$\sigma^* = \sqrt{\frac{N}{N-1} s_X^2} \pm \sqrt{\frac{N}{2(N-1)^2} s_X^2} \quad (16)$$

where $s_X^2 = \overline{X^2} - \bar{X}^2$ is the sample variance.

To determine which of both models agrees best with the given data, as obtained at a certain pressure and given the barostat and the barostat relaxation time, we used the ratio

$$R = \frac{\text{prob}(G | X, I)}{\text{prob}(P | X, I)} \quad (17)$$

as the criterion. Here, the numerator $\text{prob}(G | X, I)$ expresses the probability that the data can be explained by the Gaussian model, while the denominator $\text{prob}(P | X, I)$ expresses the probability that the data can be explained by the Poisson model. If $R > 1$, the data supports the Gaussian model, whereas if $R < 1$, the Poisson model is preferred. The preference for one model over another, based on the relative magnitude of the

applied pressure and the LP-to-CP transition pressure, is employed in the dynamical treatment found in section 4.3.

■ ASSOCIATED CONTENT

Supporting Information

The Supporting Information is available free of charge on the ACS Publications website at DOI: 10.1021/acs.jctc.5b00748.

Hamiltonian derivation of equations of motion implementing pressure coupling, a tabular overview of simulated cell parameters and free energy landscapes, and a derivation of the best estimators and their corresponding error for the two models explaining the LP-to-CP transition in MIL-53(Al). (PDF)

■ AUTHOR INFORMATION

Corresponding Author

*E-mail: Veronique.VanSpeybroeck@UGent.be.

Notes

The authors declare no competing financial interest.

■ ACKNOWLEDGMENTS

This work is supported by the Fund for Scientific Research Flanders (FWO), the Research Board of Ghent University (BOF), and BELSPO in the frame of IAP/7/05. Funding was also received from the European Union's Horizon 2020 research and innovation programme [consolidator ERC grant agreement no. 647755 – DYNPOR (2015–2020)]. Computational resources (Stevin Supercomputer Infrastructure), and services were provided by Ghent University. We would also like to thank R. Demuyne, M. E. Tuckerman, M. Parrinello, Wm. G. Hoover, and C. G. Hoover for insightful and stimulating discussions.

■ REFERENCES

- (1) Düren, T.; Bae, Y.-S.; Snurr, R. Q. *Chem. Soc. Rev.* **2009**, *38*, 1237–1247.
- (2) Karplus, M.; McCammon, J. A. *Nat. Struct. Biol.* **2002**, *9*, 646–652.
- (3) Tuckerman, M. E.; Martyna, G. J. *J. Phys. Chem. B* **2000**, *104*, 159–178.
- (4) Alder, B. J.; Wainwright, T. E. *J. Chem. Phys.* **1959**, *31*, 459–466.
- (5) Harvey, S. C.; Tan, R. K.-Z.; Cheatham, T. E., III. *J. Comput. Chem.* **1998**, *19*, 726–740.
- (6) Chiu, S. W.; Clark, M.; Subramaniam, S.; Jakobsson, E. *J. Comput. Chem.* **2000**, *21*, 121–131.
- (7) Page, A. J.; Isomoto, T.; Knaup, J. M.; Irle, S.; Morokuma, K. *J. Chem. Theory Comput.* **2012**, *8*, 4019–4028.
- (8) Basconi, J. E.; Shirts, M. R. *J. Chem. Theory Comput.* **2013**, *9*, 2887–2899.
- (9) Feller, S. E.; Zhang, Y.; Pastor, R. W.; Brooks, B. R. *J. Chem. Phys.* **1995**, *103*, 4613–4621.
- (10) Turq, P.; Lantelme, F.; Friedman, H. L. *J. Chem. Phys.* **1977**, *66*, 3039–3044.
- (11) Bussi, G.; Donadio, D.; Parrinello, M. *J. Chem. Phys.* **2007**, *126*, 014101.
- (12) Bussi, G.; Parrinello, M. *Phys. Rev. E: Stat. Nonlin. Soft Matter Phys.* **2007**, *75*, 056707.
- (13) Bussi, G.; Parrinello, M. *Comput. Phys. Commun.* **2008**, *179*, 26–29.
- (14) Bussi, G.; Zykova-Timan, T.; Parrinello, M. *J. Chem. Phys.* **2009**, *130*, 074101.
- (15) Ceriotti, M.; Bussi, G.; Parrinello, M. *Phys. Rev. Lett.* **2009**, *102*, 020601.

- (16) Ceriotti, M.; Parrinello, M. *Procedia Comput. Sci.* **2010**, *1*, 1607–1614.
- (17) Ceriotti, M.; Bussi, G.; Parrinello, M. *J. Chem. Theory Comput.* **2010**, *6*, 1170–1180.
- (18) Andersen, H. C. *J. Chem. Phys.* **1980**, *72*, 2384–2393.
- (19) Berendsen, H. J. C.; Postma, J. P. M.; van Gunsteren, W. F.; DiNola, A.; Haak, J. R. *J. Chem. Phys.* **1984**, *81*, 3684–3690.
- (20) Hoover, W. G.; Ladd, A. J. C.; Moran, B. *Phys. Rev. Lett.* **1982**, *48*, 1818–1820.
- (21) Evans, D. J.; Morriss, G. P. *Chem. Phys.* **1983**, *77*, 63–66.
- (22) Haile, J. M.; Gupta, S. J. *Chem. Phys.* **1983**, *79*, 3067–3076.
- (23) Nosé, S. *Mol. Phys.* **1984**, *52*, 255–268.
- (24) Nosé, S. *J. Chem. Phys.* **1984**, *81*, 511–519.
- (25) Hoover, W. G. *Phys. Rev. A: At., Mol., Opt. Phys.* **1985**, *31*, 1695–1697.
- (26) Nosé, S. *Mol. Phys.* **1986**, *57*, 187–191.
- (27) Martyna, G. J.; Klein, M. L.; Tuckerman, M. E. *J. Chem. Phys.* **1992**, *97*, 2635–2643.
- (28) Morishita, T. *Mol. Phys.* **2010**, *108*, 1337–1347.
- (29) Soddemann, T.; Dünweg, B.; Kremer, K. *Phys. Rev. E: Stat. Phys., Plasmas, Fluids, Relat. Interdiscip. Top.* **2003**, *68*, 046702.
- (30) Campisi, M.; Hänggi, P. *J. Phys. Chem. B* **2013**, *117*, 12829–12835.
- (31) Patra, P. K.; Bhattacharya, B. *J. Chem. Phys.* **2014**, *140*, 064106.
- (32) Parrinello, M.; Rahman, A. *Phys. Rev. Lett.* **1980**, *45*, 1196–1199.
- (33) Parrinello, M.; Rahman, A. *J. Appl. Phys.* **1981**, *52*, 7182–7190.
- (34) Nosé, S.; Klein, M. L. *Mol. Phys.* **1983**, *50*, 1055–1076.
- (35) Wentzcovitch, R. M. *Phys. Rev. B: Condens. Matter Mater. Phys.* **1991**, *44*, 2358–2361.
- (36) Lill, J. V.; Broughton, J. Q. *Phys. Rev. B: Condens. Matter Mater. Phys.* **1992**, *46*, 12068–12071.
- (37) Hoover, W. G. *Phys. Rev. A: At., Mol., Opt. Phys.* **1986**, *34*, 2499–2500.
- (38) Melchionna, S.; Ciccotti, G.; Holian, B. L. *Mol. Phys.* **1993**, *78*, 533–544.
- (39) Martyna, G. J.; Tobias, D. J.; Klein, M. L. *J. Chem. Phys.* **1994**, *101*, 4177–4189.
- (40) Martyna, G. J.; Tuckerman, M. E.; Tobias, D. J.; Klein, M. L. *Mol. Phys.* **1996**, *87*, 1117–1157.
- (41) Quigley, D.; Probert, M. I. J. *J. Chem. Phys.* **2004**, *120*, 11432–11441.
- (42) Zhou, H.-C.; Long, J. R.; Yaghi, O. M. *Chem. Rev.* **2012**, *112*, 673–674.
- (43) Rowsell, J. L. C.; Millward, A. R.; Park, K. S.; Yaghi, O. M. *J. Am. Chem. Soc.* **2004**, *126*, 5666–5667.
- (44) Gascon, J.; Hernández-Alonso, M. D.; Almeida, A. R.; van Klink, G. P. M.; Kapteijn, F.; Mul, G. *ChemSusChem* **2008**, *1*, 981–983.
- (45) Biswas, S.; Vanpoucke, D. E. P.; Verstraelen, T.; Vandichel, M.; Couck, S.; Leus, K.; Liu, Y.-Y.; Waroquier, M.; Van Speybroeck, V.; Denayer, J. F. M.; Van Der Voort, P. J. *Phys. Chem. C* **2013**, *117*, 22784–22796.
- (46) Li, H.; Eddaoudi, M.; O’Keeffe, M.; Yaghi, O. M. *Nature* **1999**, *402*, 276–279.
- (47) Eddaoudi, M.; Kim, J.; Rosi, N.; Vodak, D.; Wachter, J.; O’Keeffe, M.; Yaghi, O. M. *Science* **2002**, *295*, 469–472.
- (48) Long, J. R.; Yaghi, O. M. *Chem. Soc. Rev.* **2009**, *38*, 1213–1214.
- (49) Kitagawa, S.; Kitaura, R.; Noro, S.-i. *Angew. Chem., Int. Ed.* **2004**, *43*, 2334–2375.
- (50) Kitagawa, S.; Noro, S.-i.; Nakamura, T. *Chem. Commun.* **2006**, 701–707.
- (51) Trung, T. K.; Trens, P.; Tanchoux, N.; Bourrelly, S.; Llewellyn, P. L.; Loera-Serna, S.; Serre, C.; Loiseau, T.; Fajula, F.; Férey, G. *J. Am. Chem. Soc.* **2008**, *130*, 16926–16932.
- (52) Tranchemontagne, D. J.; Mendoza-Cortés, J. L.; O’Keeffe, M.; Yaghi, O. M. *Chem. Soc. Rev.* **2009**, *38*, 1257–1283.
- (53) Perry, J. J., IV; Perman, J. A.; Zaworotko, M. J. *Chem. Soc. Rev.* **2009**, *38*, 1400–1417.
- (54) Meek, S. T.; Greathouse, J. A.; Allendorf, M. D. *Adv. Mater.* **2011**, *23*, 249–267.
- (55) Férey, G.; Serre, C. *Chem. Soc. Rev.* **2009**, *38*, 1380–1399.
- (56) Férey, G.; Serre, C.; Devic, T.; Maurin, G.; Jobic, H.; Llewellyn, P. L.; De Weireld, G.; Vimont, A.; Daturi, M.; Chang, J.-S. *Chem. Soc. Rev.* **2011**, *40*, 550–562.
- (57) Schneemann, A.; Bon, V.; Schwedler, I.; Senkovska, I.; Kaskel, S.; Fischer, R. A. *Chem. Soc. Rev.* **2014**, *43*, 6062–6096.
- (58) Bazer-Bachi, D.; Assié, L.; Lecocq, V.; Harbuzaru, B.; Falk, V. *Powder Technol.* **2014**, *255*, 52–59.
- (59) Yot, P. G.; Boudene, Z.; Macia, J.; Granier, D.; Vanduyfhuys, L.; Verstraelen, T.; Van Speybroeck, V.; Devic, T.; Serre, C.; Férey, G.; Stock, N.; Maurin, G. *Chem. Commun.* **2014**, *50*, 9462–9464.
- (60) Gagnon, K. J.; Beavers, C. M.; Clearfield, A. J. *Am. Chem. Soc.* **2013**, *135*, 1252–1255.
- (61) Ortiz, G.; Nouali, H.; Marichal, C.; Chaplais, G.; Patarin, J. *Phys. Chem. Chem. Phys.* **2013**, *15*, 4888–4891.
- (62) Yot, P. G.; Ma, Q.; Haines, J.; Yang, Q.; Ghoufi, A.; Devic, T.; Serre, C.; Dmitriev, V.; Férey, G.; Zhong, C.; Maurin, G. *Chem. Sci.* **2012**, *3*, 1100–1104.
- (63) Ma, Q.; Yang, Q.; Ghoufi, A.; Férey, G.; Zhong, C.; Maurin, G. *Dalton Trans.* **2012**, *41*, 3915–3919.
- (64) Ghoufi, A.; Subercaze, A.; Ma, Q.; Yot, P. G.; Ke, Y.; Puente-Orench, I.; Devic, T.; Guillerme, V.; Zhong, C.; Serre, C.; Férey, G.; Maurin, G. *J. Phys. Chem. C* **2012**, *116*, 13289–13295.
- (65) Liu, Y.; Her, J.-H.; Dailly, A.; Ramirez-Cuesta, A. J.; Neumann, D. A.; Brown, C. M. *J. Am. Chem. Soc.* **2008**, *130*, 11813–11818.
- (66) Beurroies, I.; Boulhout, M.; Llewellyn, P. L.; Kuchta, B.; Férey, G.; Serre, C.; Denoyel, R. *Angew. Chem., Int. Ed.* **2010**, *49*, 7526–7529.
- (67) Rowsell, J. L. C.; Spencer, E. C.; Eckert, J.; Howard, J. A. K.; Yaghi, O. M. *Science* **2005**, *309*, 1350–1354.
- (68) Bahr, D. F.; Reid, J. A.; Mook, W. M.; Bauer, C. A.; Stumpf, R.; Skulan, A. J.; Moody, N. R.; Simmons, B. A.; Shindel, M. M.; Allendorf, M. D. *Phys. Rev. B: Condens. Matter Mater. Phys.* **2007**, *76*, 184106.
- (69) Tan, J. C.; Cheetham, A. K. *Chem. Soc. Rev.* **2011**, *40*, 1059–1080.
- (70) Ford, D. C.; Dubbeldam, D.; Snurr, R. Q.; Künzel, V.; Wehring, M.; Stallmach, F.; Kärger, J.; Müller, U. J. *Phys. Chem. Lett.* **2012**, *3*, 930–933.
- (71) Rosenbach, N., Jr.; Jobic, H.; Ghoufi, A.; Salles, F.; Maurin, G.; Bourrelly, S.; Llewellyn, P. L.; Devic, T.; Serre, C.; Férey, G. *Angew. Chem., Int. Ed.* **2008**, *47*, 6611–6615.
- (72) Rosenbach, N., Jr.; Jobic, H.; Ghoufi, A.; Devic, T.; Koza, M. M.; Ramsahye, N.; Mota, C. J.; Serre, C.; Maurin, G. *J. Phys. Chem. C* **2014**, *118*, 14471–14477.
- (73) Babarao, R.; Jiang, J. *Langmuir* **2008**, *24*, 5474–5484.
- (74) Salles, F.; Jobic, H.; Ghoufi, A.; Llewellyn, P. L.; Serre, C.; Bourrelly, S.; Férey, G.; Maurin, G. *Angew. Chem.* **2009**, *121*, 8485–8489.
- (75) Paesani, F. J. *Phys. Chem. C* **2013**, *117*, 19508–19516.
- (76) Greathouse, J. A.; Allendorf, M. D. *J. Am. Chem. Soc.* **2006**, *128*, 10678–10679.
- (77) Tafipolsky, M.; Schmid, R. J. *Phys. Chem. B* **2009**, *113*, 1341–1352.
- (78) Ghoufi, A.; Maurin, G. *J. Phys. Chem. C* **2010**, *114*, 6496–6502.
- (79) Tadmor, E. B.; Miller, R. E. *Modeling Materials: Continuum, Atomistic and Multiscale Techniques*; Cambridge University Press: Cambridge, 2011; pp 57–58.
- (80) Todorov, I. T.; Smith, W.; Trachenko, K.; Dove, M. T. *J. Mater. Chem.* **2006**, *16*, 1911–1918.
- (81) Plimpton, S. J. *Comput. Phys.* **1995**, *117*, 1–19.
- (82) VandeVondele, J.; Krack, M.; Mohamed, F.; Parrinello, M.; Chassaing, T.; Hutter, J. *Comput. Phys. Commun.* **2005**, *167*, 103–128.
- (83) Verstraelen, T.; Vanduyfhuys, L.; Vandenbrande, S.; Rogge, S. M. J. *Yaff, yet another force field*. <http://molmod.ugent.be/software/>.
- (84) Holian, B. L.; De Groot, A. J.; Hoover, W. G.; Hoover, C. G. *Phys. Rev. A: At., Mol., Opt. Phys.* **1990**, *41*, 4552–4553.
- (85) Toxvaerd, S. *Mol. Phys.* **1991**, *72*, 159–168.

- (86) Lippert, R. A.; Predescu, C.; Ierardi, D. J.; Mackenzie, K. M.; Eastwood, M. P.; Dror, R. O.; Shaw, D. E. *J. Chem. Phys.* **2013**, *139*, 164106.
- (87) Morishita, T. *J. Chem. Phys.* **2000**, *113*, 2976–2982.
- (88) Tuckerman, M. E.; Liu, Y.; Ciccotti, G.; Martyna, G. J. *J. Chem. Phys.* **2001**, *115*, 1678–1702.
- (89) du Bourg, L. B.; Ortiz, A. U.; Boutin, A.; Coudert, F.-X. *APL Mater.* **2014**, *2*, 124110.
- (90) Kirkwood, J. G. *J. Chem. Phys.* **1935**, *3*, 300–313.
- (91) Kittel, C. *Introduction to Solid State Physics*, 8th ed.; John Wiley & Sons, Inc., 2005; pp 80–81.
- (92) Hill, R. *Proc. Phys. Soc., London, Sect. A* **1952**, *65*, 349–354.
- (93) Landau, L. D.; Lifshitz, E. *Statistical Physics, Part 1*, 3rd ed.; Elsevier: Oxford, 1980; pp 338–345.
- (94) Vanduyfhuys, L.; Verstraelen, T.; Vandichel, M.; Waroquier, M.; Van Speybroeck, V. *J. Chem. Theory Comput.* **2012**, *8*, 3217–3231.
- (95) Vanduyfhuys, L.; Vandenbrande, S.; Verstraelen, T.; Schmid, R.; Waroquier, M.; Van Speybroeck, V. *J. Comput. Chem.* **2015**, *36*, 1015–1027.
- (96) Humphrey, W.; Dalke, A.; Schulten, K. *J. Mol. Graphics* **1996**, *14*, 33–38.
- (97) Ortiz, A. U.; Boutin, A.; Fuchs, A. H.; Coudert, F.-X. *Phys. Rev. Lett.* **2012**, *109*, 195502.
- (98) Serre, C.; Bourrelly, S.; Vimont, A.; Ramsahye, N. A.; Maurin, G.; Llewellyn, P. L.; Daturi, M.; Filinchuk, Y.; Leynaud, O.; Barnes, P.; Férey, G. *Adv. Mater.* **2007**, *19*, 2246–2251.
- (99) IUPAC Gold Book, *Torsion angle*. <http://goldbook.iupac.org/T06406.html>.
- (100) Bolhuis, P. G.; Chandler, D.; Dellago, C.; Geissler, P. L. *Annu. Rev. Phys. Chem.* **2002**, *53*, 291–318.
- (101) E, W.; Vanden-Eijnden, E. *J. Stat. Phys.* **2006**, *123*, 503–523.
- (102) Ghysels, A.; Vanduyfhuys, L.; Vandichel, M.; Waroquier, M.; Van Speybroeck, V.; Smit, B. *J. Phys. Chem. C* **2013**, *117*, 11540–11554.
- (103) Vanduyfhuys, L.; Ghysels, A.; Rogge, S. M. J.; Demuyne, R.; Van Speybroeck, V. *Mol. Simul.* **2015**, *41*, 1311–1328.
- (104) Rodriguez, J.; Beurroies, I.; Loiseau, T.; Denoyel, R.; Llewellyn, P. L. *Angew. Chem., Int. Ed.* **2015**, *54*, 4626–4630.
- (105) Samanta, A.; Furuta, T.; Li, J. *J. Chem. Phys.* **2006**, *125*, 084714.
- (106) Mattesini, M.; Soler, J. M.; Ynduráin, F. *Phys. Rev. B: Condens. Matter Mater. Phys.* **2006**, *73*, 094111.
- (107) Zhou, W.; Yildirim, T. *Phys. Rev. B: Condens. Matter Mater. Phys.* **2006**, *74*, 180301.
- (108) Han, S. S.; Goddard, W. A., III. *J. Phys. Chem. C* **2007**, *111*, 15185–15191.
- (109) Greathouse, J. A.; Allendorf, M. D. *J. Phys. Chem. C* **2008**, *112*, 5795–5802.
- (110) Yang, L.-M.; Vajeeston, P.; Ravindran, P.; Fjellvåg, H.; Tilset, M. *Inorg. Chem.* **2010**, *49*, 10283–10290.
- (111) Lukose, B.; Supronowicz, B.; St. Petkov, P.; Frenzel, J.; Kuc, A. B.; Seifert, G.; Vayssilov, G. N.; Heine, T. *Phys. Status Solidi B* **2012**, *249*, 335–342.
- (112) Ghoufi, A.; Maurin, G.; Férey, G. *J. Phys. Chem. Lett.* **2010**, *1*, 2810–2815.
- (113) Jaynes, E. T. *Phys. Rev.* **1957**, *106*, 620–630.
- (114) Jaynes, E. T. *Phys. Rev.* **1957**, *108*, 171–190.